On the roles of interstitial liquid and particle shape in modulating microstructural effects in packed-bed adsorbers

Contents lists available at ScienceDirect

Chemical Engineering Research and Design

journal homepage: www.elsevier.com/locate/cherd

On the roles of interstitial liquid and particle shape in modulating microstructural effects in packed-bed adsorbers

Adam Jareteg[a], *Dario Maggiolo*[a], *Srdjan Sasic*[a], *Henrik Ström*[a,b,*]

[a] *Division of Fluid Dynamics, Department of Mechanics and Maritime Sciences, Chalmers University of Technology, SE-412 96 Gothenburg, Sweden*

[b] *Division of Energy Technology, Department of Space, Earth & Environment, Chalmers University of Technology, SE-412 96 Gothenburg, Sweden*

ARTICLE INFO

Article history:
Received 3 July 2021
Received in revised form 19 November 2021
Accepted 24 November 2021
Available online 1 December 2021

Keywords:
Packed bed
Gas cleaning
Lattice-Boltzmann
Two-phase flow
Porous media
Reactive flow

ABSTRACT

Several industrial applications use packed-bed reactors for heterogeneous processes with intermittent presence of interstitial liquid. One such example is steam-regenerated adsorption systems. Here, we computationally generate two randomly packed beds of the same voidage – one with spheres and one with cylinders – to study the role of particle shape in such a process. We analyze the geometrical characteristics and determine the flow, transport and reaction properties at the same driving pressure difference. We also establish the effect of liquid on these characteristics.

The bed of spheres exhibits 69% higher permeability due to differences in microstructure, and its shorter retention time and lower specific surface yields lower conversion in a first-order heterogeneous reaction. However, at the same flow rate, the spheres could be expected to outperform the cylinders. The bed of cylinders exhibits more pronounced local concentration variations due to a dominance of smaller pores, which are not as readily accessible to the flow. The presence of interstitial liquid reduces the permeability and significantly changes the streamwise velocity distributions inside both beds, effectively homogenizing the geometries by filling up the smaller pores. The implications of the present findings for reduced-order modelling of packed-bed adsorbers are discussed.

1. Introduction

There are many industrial applications that involve solid particles in contact with a fluid stream. One such field is gas cleaning by adsorption onto activated carbon, where the latter is present in the form of a packed bed (Schweiger, 1996; Yang et al., 2019; Brosillon et al., 2001). In the design of such beds, the choice of particle shape will influence the performance of the final application (Nemec and Levec, 2005; Dorai et al., 2015; Karthik and Buwa, 2016; Allen et al., 2013; Haddadi et al., 2016; Govender et al., 2020; Thaker et al., 2019; Zare and Hashemabadi, 2020; Nouh et al., 2010). Performance characteristics that are known to vary with the particle shape include pressure drop (Nemec and Levec, 2005; Dorai et al., 2015; Karthik and Buwa, 2016; Allen et al., 2013; Haddadi et al., 2016), conductive heat transfer (Govender et al., 2020), hot-spot formation (Zare and Hashemabadi, 2020) and efficiency in reaction (Karthik and Buwa, 2016).

Packed-bed adsorbers are cycled through various stages of operation, which may include adsorption from the gas onto the solid phase, regeneration of the solids by purging with hot steam that condenses in the bed, and cooling by non-reactive gas flows (Jareteg et al., 2020). The simultaneous presence of up to three phases (gas, solid and liquid) in combination with

* *Corresponding author.*
E-mail address: henrik.strom@chalmers.se (H. Ström).

https://doi.org/10.1016/j.cherd.2021.11.031

heat, mass and momentum transfer and sorption phenomena renders this industrial application a true multiphysics one (Groen et al., 2014).

For such complex multiphysics packed-bed processes, the particle shape will have consequences for the geometrical properties of the packed material, the flow properties through the bed, the global and local reaction rates attainable in the bed, and the role of an interstitial liquid (the condensed steam) in modulating any or all of the aforementioned effects. For example, the influence of condensed steam on the adsorption process is still not well understood, which severely limits the possibilities to develop of reduced-order models for these systems (Schweiger and LeVan, 1993; Jareteg et al., 2020; Haddadi et al., 2016). Even so, three-dimensional numerical simulations of packed-bed adsorption systems are scarce, have mostly focused on pressure-swing adsorption and have treated the beds at a macroscopic scale (Gautier et al., 2018a,b; Nouh et al., 2010; Rambabu et al., 2014). Particle-resolved simulations of steam-regenerated packed-bed temperature-swing adsorption have not been attempted, because of the challenges involved in untangling the many coupled multiphysics phenomena. Our ambition here is to take a first step towards understanding the role of the particle shape and the interstitial liquid in modulating the microstructural effects in packed-bed adsorbers.

Due to the important role of the bed characteristics in packed-bed applications, a wide range of packings with different particle shapes have been investigated previously, where the flow (Deen et al., 2014; Nawada et al., 2017), heat (Deen et al., 2014; Singhal et al., 2017) and mass transfer (De Anna et al., 2014; Khirevich et al., 2010) have been characterized. Condensate trickling is a key aspect in trickle-bed reactors (Habtu et al., 2011), but the intermittent existence of condensate in steam-regenerated adsorbers has only been briefly investigated (Jareteg et al., 2017). However, most studies are done on a single particle type or by isolating a single physical phenomenon, and comparing results from different studies always introduces questions about comparability. When trying to determine the role of the particle shape in a multiphysics application, the complexity increases even further (Peters, 2013).

There are several reasons why a comprehensive characterization of the role of particle shape in a multiphysics application is of significant interest. Firstly, and most importantly, it can help improve performance by adequately informing the design and operation of a specific unit. However, it is also important to understand the influence of particle shape and its associated consequences for the packing (Nawada et al., 2017; Dolamore et al., 2019) on the various multiphysics phenomena when modeling packed beds with reduced-order models, such as in the development of correlations for 1D models. The possibility to replace traditional heuristics-based descriptions by computationally generated quantitative structure-transport relationships is indeed very appealing (Khirevich et al., 2010). Industrial gas cleaning units are typically very large and span an enormous range of spatial and temporal scales, indicating that reduced-order models are the only viable tools for their optimization and design (Jareteg et al., 2020). Since most of the sub-models and correlations for packed beds are developed for a specific particle type (Gnielinski, 1978; Onda et al., 1968), not seldom spherical particles, understanding the implications of particle shape-induced differences is important when applying such models to industrial units with other particle shapes.

The current work is directed towards trying to shed light on the following two questions: What are the implications for bed performance from changing particle shape in a steam-regenerated fixed-bed adsorber? Are there any fundamental differences in terms of predictability attainable in reduced-order models for beds of different particle shape? The latter question should be interpreted in the light of the possibility that differences in particle shape may provoke differences in the multiphysics phenomena taking place inside the beds.

The design of this study is conceived to enable the comparison of two different particle shapes within an otherwise identical setting. The two particle shapes chosen are spheres and cylinders. Cylindrical pellets are commonly used in activated carbon beds industrially (Jareteg et al., 2020), whereas spheres typically form the basis for correlations used in reduced-order models (Gnielinski, 1978) (where properties of non-spherical particles are expressed in a sphere-equivalent form). An in-depth analysis is performed for three important physics phenomena: (1) flow, permeability and dispersion analysis in a non-reactive bed, (2) conversion in a first-order heterogeneous process in the kinetically limited regime in a reactive bed, and (3) multiphase flow in a non-reactive bed mimicking the presence of interstitial liquid.

2. Methodology

This section describes the numerical frameworks and theoretical considerations used in the generation of the computational domains for the packed beds and for the simulation and analyses of the flow, transport, reaction and multiphase flow in the beds.

The equations solved in this work are the total continuity equation and balance equations for the momentum, solute and energy transport. The equation for mass continuity can be expressed as:

$$\frac{\partial \rho}{\partial t} + \frac{\partial \rho u_j}{\partial x_j} = 0 \tag{1}$$

where $\rho = \rho(\mathbf{x}, t)$ is the density and $u_j = u_j(\mathbf{x}, t)$, $j = x, y, z$ is the velocity in the x, y and z directions, respectively.

The momentum transport is described by:

$$\frac{\partial \rho u_i}{\partial t} + \frac{\partial \rho u_i u_j}{\partial x_j} = -\frac{\partial p}{\partial x_i} + \frac{\partial}{\partial x_j}\left(\mu \frac{\partial u_i}{\partial x_j}\right) + S_i \tag{2}$$

where $p = p(\mathbf{x}, t)$ is the pressure, μ is the dynamic viscosity, and S_i a potential source term (e.g. the driving pressure force).

Besides the mass continuity and momentum flow, solving for the concentration fields of individual species in the system requires a separate transport equation for each species. The evolution of the species concentration fields is determined by the mass flow, as:

$$\frac{\partial c}{\partial t} + \frac{\partial c u_j}{\partial x_j} = \frac{\partial}{\partial x_j}\left(D_m \frac{\partial c}{\partial x_j}\right) \tag{3}$$

where $c = c(\mathbf{x}, t)$ is the species concentration and D_m is the molecular diffusivity. The effect of heterogeneous reactions is accounted for via the boundary conditions, hence there is no reaction source term.

The final equation describes the transport of energy and is:

$$\frac{\partial \rho C_p T}{\partial t} + \frac{\partial \rho C_p T u_j}{\partial x_j} = \frac{\partial}{\partial x_j}\left(\kappa \frac{\partial T}{\partial x_j}\right) \tag{4}$$

where C_p is the specific heat, $T = T(\mathbf{x}, t)$ is the temperature and κ is the thermal conductivity.

2.1. The lattice Boltzmann method

To solve the governing equations (Eqs. (1)–(4)), the lattice Boltzmann method (LBM) is used. This numerical method is especially well suited for porous media flows and it is thus adopted for the current work (Succi, 2001). Instead of solving the above equations directly, the method is based on discretizing and solving the Boltzmann equation:

$$(\partial_t + \mathbf{v} \cdot \nabla) f = \Omega[f] \tag{5}$$

This equation describes the evolution of the single-particle distribution function $f(\mathbf{x}, \mathbf{v}, t)$, where the left-hand side describes the free advection of f while on the right hand side, Ω describes pairwise particle collisions. This operator is commonly simplified to the linear Bhatnagar–Gross–Krook (BGK) form of:

$$\Omega[f] = -\frac{1}{\tau_v}(f - f^{eq}) \tag{6}$$

where f^{eq} is the Maxwell–Boltzmann equilibrium distribution and τ_v is a characteristic relaxation time. These equations obey the governing transport equations in the limit of small Mach and Knudsen numbers. The Boltzmann equation (5) is discretized in physical and velocity space to obtain the lattice Boltzmann equation (LBE):

$$f_i(\mathbf{x} + \mathbf{c}_i \Delta t, t + \Delta t) = f_i(\mathbf{x}, t) - \frac{1}{\tau_v}\left(f_i(\mathbf{x}, t) - f_i^{eq}(\mathbf{x}, t)\right) + F_i \tag{7}$$

In this work, we use the three-dimensional 19-velocity lattice known as D3Q19. Thus, in Eq. (7), $f_i(\mathbf{x}, t)$ is the discrete single-particle distribution function and $\mathbf{c}_i$ is the discrete velocity for the ith velocity direction ($i = 0 \ldots 18$). F_i is any body force applied to the system and the discrete equilibrium distribution f_i^{eq} is expressed as:

$$f_i^{eq}(\mathbf{x}, t) = w_i \rho \left(1 + \frac{\mathbf{c}_i \cdot \mathbf{u}(\mathbf{x}, t)}{c_s^2} + \frac{(\mathbf{c}_i \cdot \mathbf{u}(\mathbf{x}, t))^2}{c_s^4} - \frac{\mathbf{u}^2(\mathbf{x}, t)}{2c_s^2}\right) \tag{8}$$

where w_i is a lattice weight and c_s is the lattice sound speed.

As a driving force to the flow, a pressure gradient ($\Delta P/L$) is applied as a body force to the simulation (Guo et al., 2002). This body force is expressed as:

$$F_i(\mathbf{x}, t) = \left(1 - \frac{1}{2\tau_v}\right) w_i \left(\frac{\mathbf{c}_i - \mathbf{u}(\mathbf{x}, t)}{c_s^2} + \frac{\mathbf{c}_i \cdot \mathbf{u}(\mathbf{x}, t)}{c_s^4}\mathbf{c}_i\right)\left(\frac{\Delta P}{L}\right) \tag{9}$$

The macroscopic properties are calculated as:

$$\rho(\mathbf{x}, t) = \sum_i f_i(\mathbf{x}, t) \tag{10}$$

$$\rho(\mathbf{x}, t)\mathbf{u}(\mathbf{x}, t) = \sum_i \mathbf{c}_i f_i(\mathbf{x}, t) + \left(\tau - \frac{1}{2}\right)\left(\frac{\Delta P}{L}\right) \tag{11}$$

Eq. (7), which describes the evolution of the discrete single-particle distribution, is also used to describe scalar transport. For this purpose, a new distribution, g_i, is introduced and solved for using Eq. (7). The only difference is that the external forcing term, F_i, is excluded, since the scalar is simply transported by the flow. The corresponding equilibrium distribution function for the scalar, g_i^{eq}, is evaluated corresponding to Eq. (8). The concentration is finally calculated as:

$$c(\mathbf{x}, t) = \sum_i g_i(\mathbf{x}, t) \tag{12}$$

The phenomenon where a gas phase species vanishes at the external surface of the particles in the bed (e.g. by reaction or adsorption) is modelled as a first-order heterogeneous reaction. The reactive boundary condition is a linear surface reaction that is implemented as a Robin boundary condition according to Huang and Yong (2015):

$$\alpha_1 \frac{\partial c}{\partial \boldsymbol{n}} = -(\alpha_2 c - \alpha_3) \tag{13}$$

where α_x ($x = 1, b, 3$) defines the equilibrium and rate constants, such that the final boundary condition is of the form (Maggiolo et al., 2020):

$$D_m \frac{\partial c}{\partial \boldsymbol{n}} = -k(c - c_0) \tag{14}$$

where $\alpha_1 = D_m$, $\alpha_2 = k$ (where k is the reaction rate constant), and $\alpha_3 = kc_0$ (where $c_0 = 1$). For this simulation, α_1 is defined so that the Schmidt number ($Sc = \mu/\rho D_m$) becomes unity ($\alpha_1 = 1/6$) and the fluid Péclet number ($Pe = \overline{u}_x d_p / D_m$) thus equals the bed Reynolds number (as will be defined later in Eq. (19) and shown to be of $\mathcal{O}(0.1 - 1)$). α_2 and α_3 are defined to yield a Damköhler number ($Da = k/\overline{u}_x$) $\ll 1$ so that the system is kinetically controlled ($\alpha_2 = \alpha_3 = 2 \times 10^{-5}$).

For the modeling of the gas–liquid system, the two-phase Shan–Chen (Shan and Chen, 1993) scheme is used with a thermo-fluid model by Zhang and Tian (2008). The velocity calculation in Eq. (11) is altered by the interaction force F_{sc} and becomes (Shan and Chen, 1993):

$$\rho(\mathbf{x}, t)u_i(\mathbf{x}, t) = \sum_i \mathbf{c}_i f_i(\mathbf{x}, t) + \left(\tau - \frac{1}{2}\right)\left(\frac{\Delta P}{L} + F_{sc}\right) \tag{15}$$

The interaction force F_{sc} is calculated as:

$$F_{sc} = -G\Psi(\mathbf{x}, t)\sum_i w_i \Psi(\mathbf{x} + \mathbf{c}_i \Delta t, t)\mathbf{c}_i \tag{16}$$

where $G = -7.0$ is the Shan–Chen parameter that determines the interaction strength and $\Psi(\mathbf{x}, t) = e^{-1/\rho}$ is the density-dependent pseudopotential describing both long-range attraction and short-range repulsion (Maggiolo et al., 2019) and formulated so as to ensure thermodynamical consistency (Sbragaglia and Shan, 2011). Here, we stress that the computational framework is formulated in a non-dimensional manner, so that relevant quantities are defined as ratios and via characteristic numbers.

A non-ideal equation of state relates density and temperature as:

$$P = \rho T + \frac{G}{2} c_s^2 \Psi^2 \tag{17}$$

The moving gas–liquid contact line (90°) is implemented through a proper averaging of the density-dependent function Ψ close to the three-phase contact point (De Maio et al., 2011):

$$\Psi_{wall} = \frac{1}{N}\sum_{N}\Psi + \Delta_w \tag{18}$$

The density-dependent function Ψ_{wall} mimics the van-der-Waals intermolecular force at the solid wall by using the N nearest fluid computational nodes. By adjusting the parameter Δ_w, it is possible to represent different contact angles at the macroscopic scale.

2.2. Bed generation

The computational geometries are generated in the open 3D-rendering software Blender (Blender, 2021). Blender has a physics module that allows for mesh interactions and, together with the gravity body forcing, this allows mesh objects to fall freely and collide with each other. This approach is here adopted for cylindrical and spherical particles respectively. Both particle shapes use the same characteristic particle diameter, and the beds are randomly packed.

The three main steps of the methodology are highlighted in Fig. 1. Initially, a large container, which is open at the top with solid sides and bottom, is created and objects of the desired shape are spawned at random positions and with random orientation within a horizontal plane some distance above the container. A downward body force is applied to the spawned objects, which then proceed to fall into the container. Although the objects are spawned one at a time, their subsequent drop into the container takes some finite time. For this reason, newly inserted objects may interact with already falling objects and the final packing is not necessarily identical to the one that would have been generated if every object would have been allowed to come to rest before the next object was spawned. Furthermore, the container was not shaken or vibrated during the packing process, to avoid global alignment patterns that otherwise could emerge, particularly for the cylinders (Zhang et al., 2006). This simulation strategy was chosen to realistically represent the industrial bed filling process, where activated carbon particles are poured into the adsorber beds (Boccardo et al., 2015; Jareteg, 2021). Some sensitivity to the applied packing method is however to be expected with regard to the macroscopic bed properties (especially for the bed of cylinders), and we shall return to this question in the analysis of the generated bed geometries in Section 3.1.

When the container is full (Fig. 1a) the process is stopped. Thereafter, a representative geometry is cut out of the middle of the bed (Fig. 1b) which becomes the input (Fig. 1c) for an algorithm to transform the resulting surface mesh into a lattice Boltzmann mesh. The presence of nearby walls (horizontally and on the bottom) gives rise to ordered structures in the packing, the effects of which persist over distances equal to a few particle diameters into the container (Dixon, 1988; Zou and Yu, 1995; Mueller, 2005). In the present work, the computational domain is extracted from a location six characteristic particle diameters away from the walls, where the influence from the walls on the bed porosity is expected to be $\lesssim$1.2% for the spheres and $\lesssim$2.5% for the cylinders (Dixon, 1988). Furthermore, the size of the extracted computational domain should be chosen such that the simulations adequately reflect the macroscopic properties of the packed bed. In this work, the computational domain is $4\times4\times4$ characteristic particle diameters, which is slightly larger than typical domains used in particle-resolved packed-bed simulations in the literature (Tabib et al., 2013; Tavassoli et al., 2015; Schulze et al., 2017). The resulting two geometries used in this study are shown in Fig. 1(panels d and e). The computational grid also includes an empty inlet section that is added upstream the porous section of the domain, and a similar empty outlet section downstream. The computational domain thus represents the porous media as an open system (Nauman and Nigam, 2005).

2.3. Case setup and analysis description

2.3.1. Bed characterization

Basic flow and geometrical properties are extracted from a steady-state simulation with only momentum transport, where the same pressure drop, $\Delta p/L$, is applied in the main flow direction for both geometries. This same pressure drop is used for all the other simulations as well. In the two other coordinate directions, a free-slip boundary condition is used.

In the analysis to follow, the bed Reynolds number is based on the characteristic particle diameter (d_p) and the mean interstitial velocity in the streamwise direction ($\overline{u}_x$), and is evaluated as:

$$Re_p = \frac{d_p \overline{u}_x \rho}{\mu} \tag{19}$$

The permeability, K, is based on Darcy's law and expressed as:

$$K = \frac{\overline{u}_x \mu L}{\Delta p} \tag{20}$$

The rationale for comparing the two beds at the same pressure drop, rather than at the same bed Reynolds number, stems from the fact that the industrial processes of interest in the current work are typically pressure-drop limited. From the industrial perspective, it is thus the attainable performance at a given pressure drop that is most relevant.

The pore-size distribution is evaluated based on an algorithm from Rabbani et al. (2014), which calculates a pore-size distribution from a 2D slice of binary information. Several such 2D slices of the domain are then analyzed to form the complete 3D pore-size distribution. Fig. 2 presents two examples of 2D slices of the geometry, used in the pore-size distribution calculations. Each geometry is sliced into 50 such 2D slices to build the final 3D distribution.

2.3.2. Passive scalar

The transport of a passive scalar is used to characterize the two geometries by determining the residence time distribution, $E(t)$, from a simulation where a step change in the inlet passive scalar concentration is applied at $t=0$:

$$E(t) = \frac{1}{c_{in}}\frac{\partial c}{\partial t}\bigg|_{out} \tag{21}$$

Here, the time t is scaled with the corresponding advective time scale $\tau = L/\overline{u}_x$ for the geometry in question. Also the average, maximum and minimum concentrations in planes perpendicular to the main flow direction are extracted at time $t=\tau/2$.

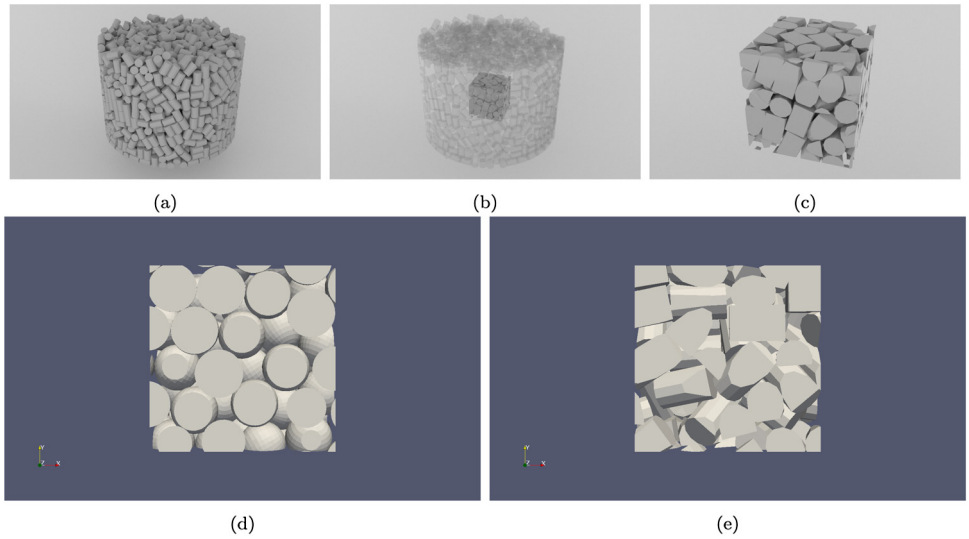

Fig. 1 – Illustration of the bed generation procedure and the two computational geometries: (a) container packed with particles, (b) a square box far away from the container walls is chosen as the representative geometry, (c) the resulting cut-out of the bed to be used in the subsequent simulations, (d) illustration of the computational domain for the packed bed of spheres, (e) illustration of the computational domain for the packed bed of cylinders.

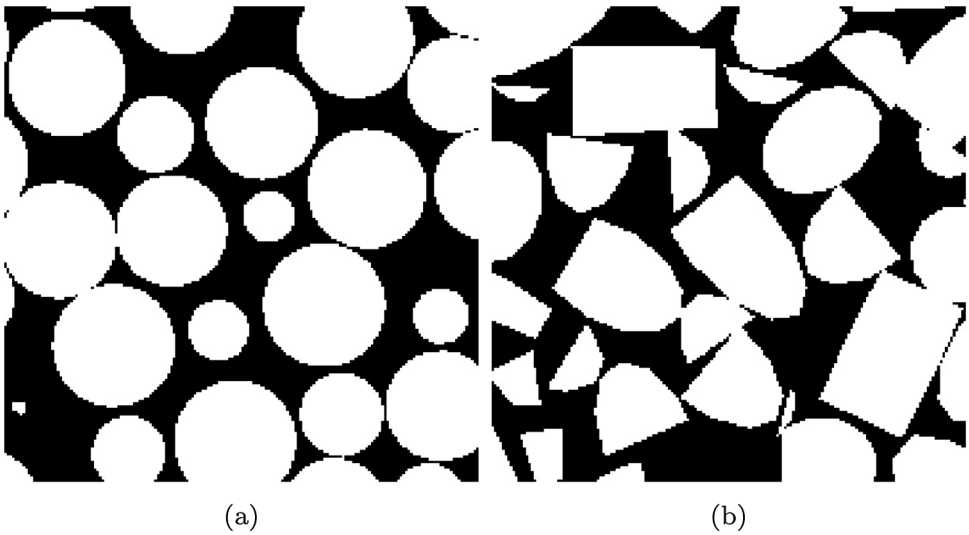

Fig. 2 – Illustration of 2D slices used in determining the 3D pore size distribution for the two computational geometries: (a) spheres, (b) cylinders.

2.4. *Reactive scalar*

The simulations for the reactive cases are performed in the same way as the passive scalar simulations, but with surface reactions enabled. The results are extracted once the solution is at a steady state, defined as when the outlet concentration does not change with time. The same value for k is used in all reactive simulations (cf. Eq. (14)).

The conversion, χ, is then calculated as:

$$\chi = \frac{1 - \phi_o}{\phi_i} \tag{22}$$

where ϕ_o and ϕ_i are the mass-flow weighted averages of the scalar concentration at the outlet and the inlet, respectively. Note that this approach inherently assumes that diffusional effects at the outlet and inlet, as well as the hydrodynamic dispersion, can be neglected (Maggiolo et al., 2020).

To enable a comprehensive analysis of the performance of the reactive system, we choose to compare the predictions in the fully resolved simulations to an ideal one-dimensional representation. Such a representation can be derived for a plug-flow reactor with an irreversible, first-order surface reaction in a porous media, and the predicted concentration profile then becomes:

$$c(x) = c_{in} \exp\left(\frac{-kax}{\overline{u}_x}\right) \tag{23}$$

Here, a is the domain-averaged specific surface and x is the position at which the average concentration in the cross-section normal to the streamwise direction is $c(x)$. c_{in} is the concentration at the domain inlet. In this way, it becomes possible to directly assess streamwise concentration profiles extracted from the detailed simulations against a theoretical prediction from a one-dimensional representation. For this one-dimensional model, the local conversion can thus be retrieved as:

$$\chi = 1 - \exp\left(\frac{-kax}{\overline{u}_x}\right) \tag{24}$$

In contrast to the lattice Boltzmann simulations, this model represents the porous media as a closed system (Nauman and Nigam, 2005).

2.5. *Multiphase simulation*

The multiphase simulations (involving the effect of interstitial liquid in the domain) are done with 30% liquid fraction (70% gas) and periodic boundary conditions in the streamwise direction. The simulation setup is done in such a way that this preset amount of fluid condenses as the solution is advanced in time from an initially metastable thermodynamic state. Thereafter, the simulations continue so that the liquid is allowed to run under the gravitational force. The gravitational force is applied through the same source term as the pressure force, i.e. S_i in Eq. (2) and F_i in Eq. (7). Gravitation acts in the opposite direction of the pressure force, which causes the liquid to flow counter-current to the gas flow. This setup thus mimics the downwards trickling of a liquid phase in an upwards gas flow through a packed bed of solids, which is an industrially relevant configuration in packed-bed adsorption (Jareteg et al., 2020). Results for further analysis are then extracted once steady conditions have been established.

The same method for pore-size extraction as mentioned in Section 2.3.1 is used in the extraction of the pore-size distribution from the simulations with interstitial liquid. In this analysis, the liquid is also treated as a solid material in the binary 2D images.

3. Results

This section is divided into four parts. First, the packed beds of spheres and cylinders are analyzed with respect to their geometrical characteristics and flow dynamics. Thereafter, the passive scalar simulations are used as a basis for investigating the dispersion in the two types of beds. We then turn to the reactive scalar results to determine the effect of the geometry, flow characteristics and dispersion on the conversion in a first-order heterogeneous process. Finally, we perform a comprehensive assessment of the effect of interstitial liquid on the behavior of the two bed types.

3.1. *Geometry and flow*

Before analyzing any flow simulation results, important characterizations of the different geometries can be made solely based on the geometries themselves. In Table 1, a number of important parameters are listed. Noticeably, the voidage of the packings are very similar (within 2% of each other). We emphasize that this degree of similarity can in general only be expected between spheres and cylinders of aspect ratio close to unity. The aspect ratio adopted in the current work is chosen to reflect the properties of cylinders used in a relevant industrial process (Jareteg et al., 2020). Nevertheless, working with an aspect ratio as low as 1.5 largely suppresses the influence of preferential cylinder alignment, which should be kept in mind when further analyzing the results.

The voidage of the bed of spheres agrees (within approximately 2%) with the commonly accepted random close-packing limit of 0.36 for hard spheres (Berryman, 1983; Jin and Makse, 2010; Baranau and Tallarek, 2014). We attribute the small difference to the finite resolution used in the numerical determination of the voidage (cf. Fig. 2). The voidage span in the literature for randomly packed beds of cylinders is larger

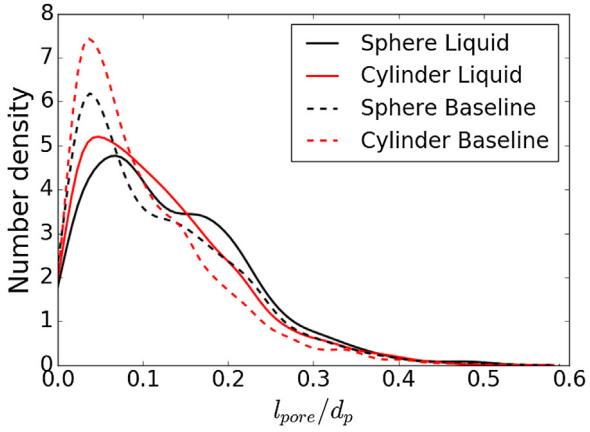

Fig. 3 – Pore size distributions for the packed beds of spheres and cylinders with ("liquid") and without ("baseline") the presence of an interstitial liquid.

than that of spheres, due to a more pronounced sensitivity to the degree of ordering and thus the packing method (Zhang et al., 2006). Random close packing of equilateral cylinders results in a bulk voidage in the range 0.279–0.364, depending on the packing method, and statistically decreases with increasing the aspect ratio of the cylinders (Zhang et al., 2006). The voidage obtained for the bed of cylinders in the current work is consistent with previous observations for cylinders of aspect ratio 1–1.2 packed without subsequent vibration (Zhang et al., 2006).

Although the bed bulk voidages are similar for the spheres and the cylinders, there are differences in the distribution of the pore sizes. The mean pore size is smaller for the cylindrical case, whereas for both cases the standard deviation of the pore size is quite significant. Fig. 3 shows the pore size distribution for both geometries (multi-phase cases are included for comparison). From the figure, two important observations can be done. Firstly, it is clear that the packed bed of cylinders yields a higher concentration of smaller pores. Secondly, the bed of spheres shows a tendency to bimodality in the distribution. After the peak at smaller pore sizes, there is a shoulder region around $l_{pore}/d_p = 0.1 - 0.2$ where the decay is reduced, indicating the existence of a cluster of pores of larger size.

The smaller pores of the cylindrical geometry results in a reduced permeability and a lower Reynolds number for the given pressure forcing (cf. Table 1). The difference in permeability is not negligible, with the bed of spherical particles having 69% higher permeability than the bed of cylinders. This difference is important for applications where the pressure drop is a limiting design factor, as a higher permeability will yield a lower pressure drop for a given flow. Consequently, a higher permeability means that one can allow a larger bed at a given flow rate and limiting pressure drop, bringing larger flexibility to the bed operation. The fact that a packed bed of non-spherical particles, such as cylinders, exhibits a lower permeability than a packed bed of spheres at the same voidage is well in line with previous findings in the literature (Nemec and Levec, 2005; Dolamore et al., 2019).

Fig. 4 illustrates the velocity distributions inside the beds, where the normalized streamwise velocity distribution (Fig. 4a) exhibits a characteristic asymmetrical and exponentially decaying velocity. Even though the pore size distributions are different in the two beds, the velocity distributions (both streamwise and crosswise, cf. Fig. 4a and b) are rather similar. These observations point to that the pore size

Table 1 – Geometrical characterization, retention time and conversion for the packed beds of spheres and cylinders. The specific surface, permeability and retention time have been made dimensionless by normalization with the results for the cylinders (the subscript c refers to *cylinders*).

Property	Variable	Spheres	Cylinders
Aspect ratio	l/d_p	–	1.5
Voidage	ε	0.352	0.346
Specific surface	a/a_c	0.90	1
Reynolds number	Re_p	0.72	0.43
Permeability	K/K_c	1.69	1
Mean of pore size distribution	μ_{pore}/d_p	11.84×10^{-2}	10.35×10^{-2}
Standard deviation of pore size distribution	σ_{pore}/d_p	9.06×10^{-2}	8.14×10^{-2}
Retention time	τ/τ_c	0.60	1
Conversion	χ	0.24	0.35

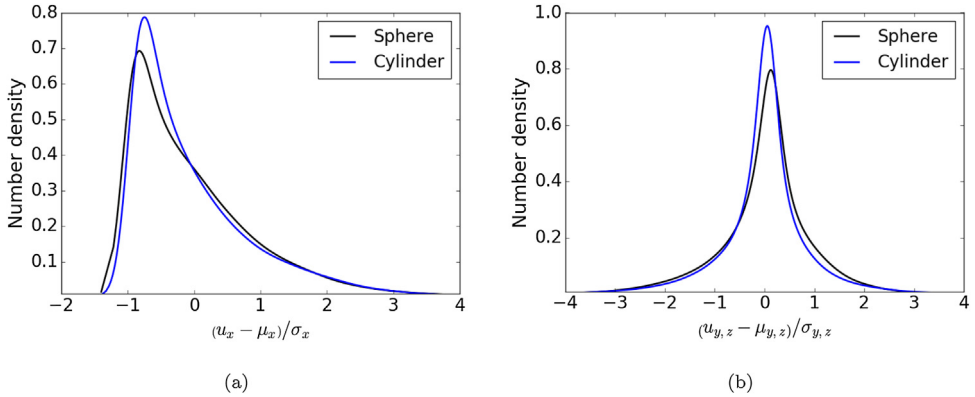

Fig. 4 – Probability distributions for the flow velocity inside a bed of cylinders or spheres: (a) streamwise velocity component, (b) crosswise velocity components.

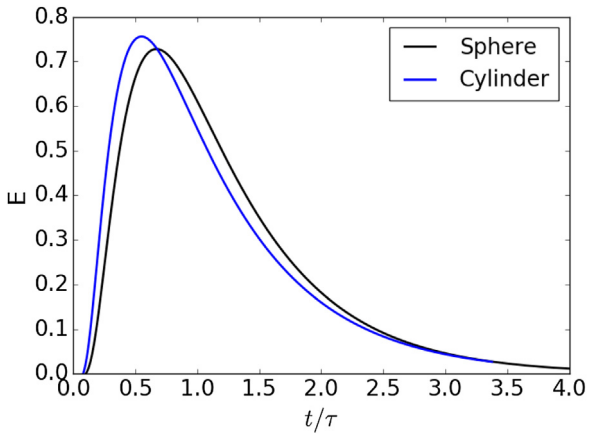

Fig. 5 – Residence time distributions as derived from passive tracer simulations in the beds of spheres and cylinders.

distribution alone does not make a good predictor for flow and dispersion properties without further analyses being done.

3.2. *Transport characteristics*

The passive scalar simulations enable the determination of dispersion properties for the two different geometries. Fig. 5 shows the residence time distributions, from which it can be seen that both beds exhibit a similar dispersive behavior for the current low-Reynolds number flow case. The bed with spherical particles shows a slightly wider distribution, indicative of slightly higher in-bed dispersion. Consequently, one would expect the bed of spheres to produce a more homogenized concentration field in the streamwise direction. This expectation is confirmed in Fig. 6, where the average concentration as well as the concentration span in every cross-section throughout the computational domain are illustrated. It can clearly be seen that the concentration variations throughout the bed are more pronounced in the bed of cylinders. Interestingly, this situation arises even though the flow through the bed of cylinders is characterized by a lower Reynolds number, which is a flow situation where diffusional effects are more pronounced and smaller gradients therefore could be expected. In other words, the lower dispersion and higher concentration variations observed in the bed of cylinders must be an effect of the changes in geometry resulting from the packing of the different types of particles. It has for example been suggested that the possibility for cylinders to align preferentially in the bed (due to the effect of gravity upon packing of the bed) may lead to anisotropy and orientation-dependent performance (Dorai et al., 2015). Finally, the illustration provided in Fig. 7 highlights the complexities involved in analyzing the differences in transport characteristics in the two beds, as the maximum and minimum concentrations are found along different flow paths, separated spatially from each other in ways determined by the local microstructure.

3.3. *Performance in reaction*

A fundamental measure of the reactive properties of the two bed geometries is the conversion of a reactant over the bed. The conversion resulting from a first-order heterogeneous reaction can be found in Table 1 for both beds. It is seen that, in the bed with cylinders, the scalar is consumed to a higher degree than in the bed of spheres. However, there are a number of factors that contribute to determining the overall conversion that need to be addressed to unpack this observation.

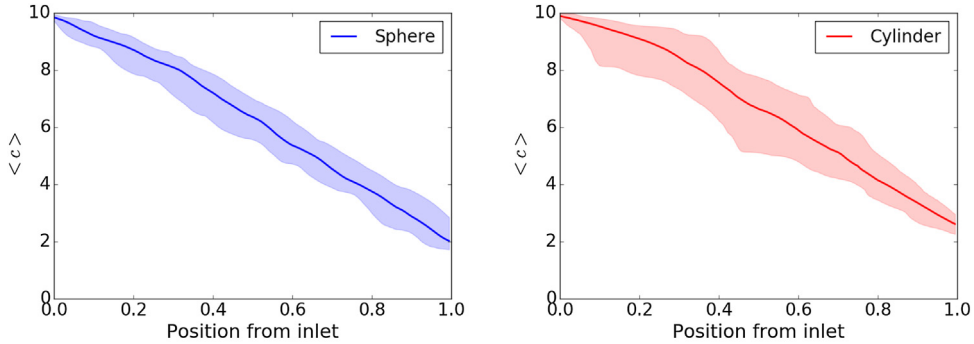

Fig. 6 – Concentration profiles for a non-reacting flow through the bed in the streamwise direction. Solid lines indicate the evolution of the cross-sectional average and the shaded region marks the (1%, 99%) concentration range in each cross section. The data has been extracted from the step tracer simulation at $t = \tau/2$, when the flow has on average reached half-way through the bed, i.e. in the absence of dispersion both profiles would show a step change in concentration in the middle of the bed and constant (higher and lower) concentrations upstream and downstream this location. Bed geometries: (a) spheres, (b) cylinders.

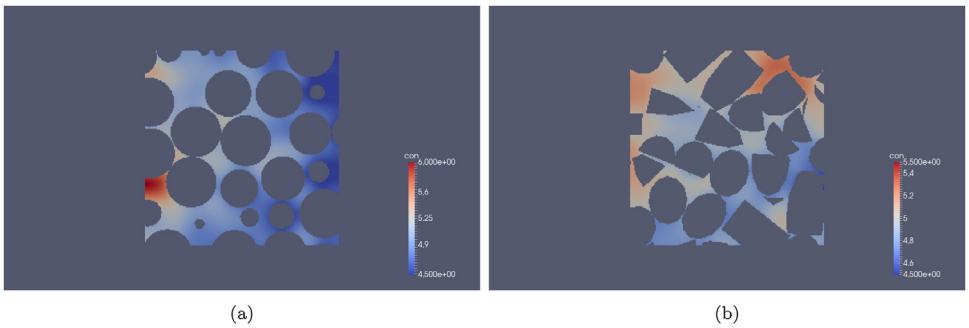

Fig. 7 – Passive tracer concentration in a cross-sectional plane normal to the streamwise direction. Bed geometries: (a) spheres, (b) cylinders.

Differences in the flow, the specific surface and the retention (contact) time all affect the conversion. The reaction rate also decays with increasing conversion (cf. Eq. (23)), and we must therefore proceed to elucidate the process from different angles for a comprehensive analysis.

Since the Reynolds number is different for the two beds, there is a difference in retention time between the cases. The contact time is around 66% longer for the cylindrical case (cf. Table 1). At the same time, the specific surface exposed in the bed of cylinders is about 11% higher. These facts imply that the product $kax/\overline{u}_x$ is approximately 84% higher for the bed of cylinders than for the bed of spheres, and therefore the conversion should expected to be higher in the former. This is also the observation that can be made when comparing the conversions attained in the two beds (cf. Table 1), the difference is however only 46%. As given by Eq. (24), the relationship between conversion and $kax/\overline{u}_x$ is not linear, but for low-to-intermediate conversions the relationship actually recovers similarity to a direct proportionality. This fact points to that the bed of cylinders is in fact performing worse than what would be expected if the reaction were not limited by mass transport (reaction-limited regime). We therefore need to turn to a detailed investigation of the concentration fields inside the two beds.

Fig. 8 shows the concentration profiles through the bed at steady state and a few important observations can be made from it. The higher conversion in the case of cylinders is seen as a lower outlet concentration (at $x/L = 1$). Both cases show only a slightly curved profile, indicative of a system where conversion is significantly lower than one (cf. Eq. (24)). However, when analyzing the local deviations from the average concentration at each cross-section, differences between the two beds become apparent. Most notably, for the cylindrical case, a substantially larger variation of concentration is found in the majority of the domain, as illustrated by the larger extent of the shaded region in Fig. 8a as compared to Fig. 8b. This variation of concentration is an indirect measure of the availability of the surfaces in the domain to the flow. In the cylindrical case, there seem to be some surfaces that do not have an equally good supply of reactant as others, in particular in comparison to the spherical case where the spread is lower. This situation arises in spite of the relatively lower Reynolds number in the bed of cylindrical particles. This observation corresponds well with the pore-size distributions found, where the cylindrical pores are both smaller on average and with a higher concentration of small pores. It is likely that the smaller pores, while allowing for the presence of an overall increased surface area, are not as readily accessible to the reactant as the larger ones, resulting in local clusters of pores with lower concentration. The fact that small pores appear where surfaces from adjacent particles are in close proximity within the beds explains why a bed of spheres (that can only touch at single points) have fewer such entities than a bed of cylinders (that may align along the same direction and meet end-face-to-end-face). It is thus possible to establish a link between particle shape via the pore-size distribution/surface accessibility to the bed transport characteristics. This phenomenon is in line with

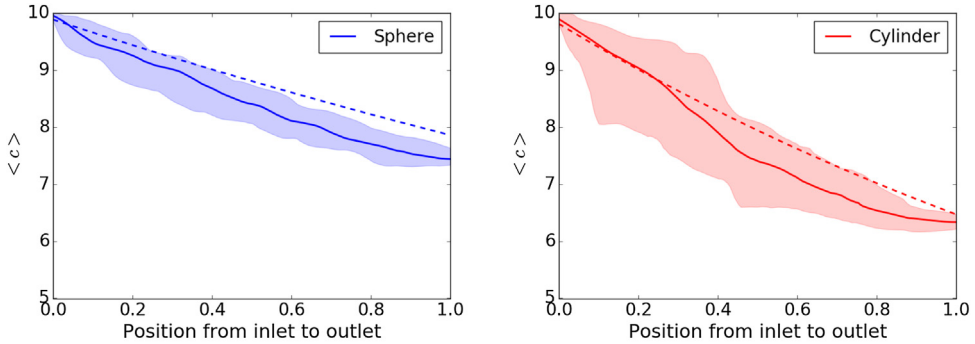

Fig. 8 – Concentration profiles for a reacting flow through the bed in the streamwise direction. Solid lines indicate the evolution of the cross-sectional average and the shaded region marks the (1%, 99%) concentration range in each cross section. The dashed lines illustrate the predictions from Eq. (23). Bed geometries: (a) spheres, (b) cylinders.

the previous analysis of the differences in transport characteristics between the two beds, and explains why the bed of cylinders does not deliver full performance improvement in reaction despite the larger specific surface and longer retention time at the same driving pressure.

Besides the regions with lower concentration, some regions show a significantly higher concentration than the average in the bed of cylindrical particles. The underlying reason must be due to some form of channeling phenomenon in the bed, where certain flow paths are in contact with surrounding surfaces for a shorter time, thus not being consumed at the same rate as the bulk flow.

The comparisons to the predictions from Eq. (23) in Fig. 8b support the previous discussion, in that the slope of the cross-sectional average varies more than the slope of the one-dimensional prediction; this behavior is indicative of variations in cross-sectional specific surface along the streamwise direction. The fact that the one-dimensional model predicts a lower conversion for the bed of spheres than the lattice Boltzmann simulations in Fig. 8a is perhaps somewhat more surprising, as dispersion generally lowers conversion for positive reaction orders. However, the difference in domain-averaged conversion is of the same order of magnitude as would be expected from allowing diffusion to take place in the exit region of the computational domain. It is known that the effect of cross-channel diffusion in the exit zone in an open system is to increase conversion (Nauman and Nigam, 2005). We thus attribute this observation to the fact that the LBM simulations describe an open system whereas the one-dimensional model describes a closed system, even though we cannot fully exclude hydrodynamic dispersion effects.

3.4. *Effect of interstitial liquid*

When a second (liquid) phase is introduced, this liquid will tend to fill smaller pores and limit and/or obstruct the flow through the bed. Consequently, the expected effect of an interstitial liquid is to reduce the permeability, and since the pressure forcing is kept constant, the Reynolds number is reduced. Table 2 shows the permeability and Reynolds number of each bed in the presence of interstitial liquid, together with the mean pore size and the standard deviation of the pore sizes. As can be seen, the Reynolds number decreases significantly for both cases as compared to the dry beds. However, the difference between the two types of beds is also greatly reduced. For the single-phase case, the Reynolds number of the geometry based on spheres was about 70% higher than the corresponding cylindrical case, while it is only about 15% higher for the multiphase case with interstitial liquid. The reason for this behavior is found in the changes to the pore size distribution that result from the presence of the liquid, i.e. the changes to the geometrical characteristics as seen by the gas. Fig. 3 also shows the pore size distribution for the multiphase cases. It can be seen that the presence of the liquid phase homogenises the two different beds due to that the liquid fills the smaller pores. This phenomenon results in the void fraction consisting to a higher degree of larger pores, something which is also reflected in the average pore sizes (Table 2).

Fig. 9 shows additional evidence of the mechanism inferred from the changes to the pore size distributions. These contour plots, delineating the regions occupied by the three phases (solid particles, liquid and gas) clearly show how the liquid fills the smaller pores and narrow gaps between particles due to surface tension effects and leaves the larger pores empty. The homogenization of the macroscopic flow properties of the different geometries due to the presence of interstitial liquid is thus an important finding that highlights a phenomenon that should be accounted for when designing bed systems where there will be a liquid present, continuously or intermittently. Packed beds for adsorption that are regenerated with steam are one such example, where there will be a recurring presence of a condensed phase inside the beds. These facts mean, for example, that the benefits of a lower permeability when using spherical particles – which is definitely present for single-phase flows – will be much reduced when a condensed phase is also present. It is also evident from Fig. 9 that the surface area of the liquid exposed to the gas, which is an important parameter in determining the evaporation rate of the remaining liquid, is determined by the packing rather than by the intrinsic particle shape, and therefore is also much more similar between the two beds than would otherwise have been the case. This area of the gas-liquid interface is one of the least well-characterized parameters in current state-of-the-art reduced-order models for steam-regenerated packed-bed adsorbers (Jareteg et al., 2020).

The interstitial liquid does not only affect the pore size distribution, but also the velocity distribution. Fig. 10 shows the velocity distributions, the same as in Fig. 4 but now with the addition of the multiphase cases. The effect on the streamwise component is significant, with the distribution going from the asymmetrical velocity distribution of the single phase, to a much more Gaussian appearance, centered around the mean

Table 2 – Geometrical characterization of the packed beds of spheres and cylinders in the presence of an interstitial liquid. The permeability has been made dimensionless by normalization with the results for the cylinders (the subscript *c* refers to *cylinders*).

Property	Variable	Sphere	Cylinder
Reynolds number	Re_p	0.15	0.13
Permeability	K/K_c	1.18	1
Mean of pore size distribution	$\mu_{pore,liq}/d_p$	13.2×10^{-2}	12.1×10^{-2}
Standard deviation of pore size distribution	$\sigma_{pore,liq}/d_p$	9.02×10^{-2}	8.60×10^{-2}

(a) (b)

Fig. 9 – Contour plots of representative 2D cross-sections of the two types of bed in the presence of interstitial liquid. Empty regions are occupied by the bed particles, whereas the light grey regions indicate voids available to the gas phase and the black regions indicate the location of the liquid phase. Bed geometries: (a) spheres, (b) cylinders.

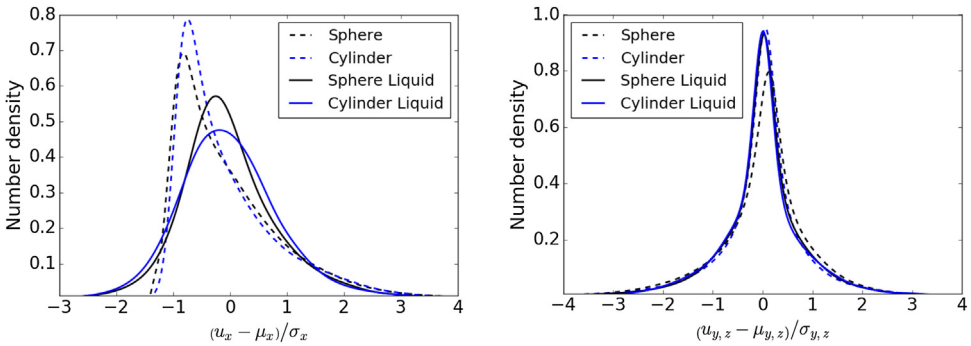

(a) (b)

Fig. 10 – Velocity distribution in the gaseous phase in the two beds in the presence of interstitial liquid: (a) streamwise velocity, (b) cross-wise velocities.

value. This observation is true for both beds and, much like for the single-phase case, both beds share great similarities. As the difference in pore size distribution does not seem to impact the velocity distribution to any great extent (cf. Fig. 4) the reason for the change must be the interaction between the liquid phase and gas phase. These observations are significant in that they highlight that reduced-order models ideally should adapt their descriptions of the flow through the bed to account for the recurrent presence of liquid in industrial cycling of packed-bed adsorbers, which is not the case in currently available models.

4. Conclusions

Two randomly packed beds (one with spheres and one with cylinders) have been computationally generated and their geometrical properties and performance characteristics in flow, transport and reaction have been established using numerical simulations. Furthermore, the effect of an interstitial liquid on the flow characteristics has also been analyzed. The aim is to elucidate the role of the particle shape on the performance of a reactor in a multiphysics application such as steam-regenerated packed-bed adsorption.

It is found that, even though the two particle shapes can be packed to achieve virtually the same voidage on a macroscopic level (at the same characteristic particle size and for close to equilateral cylinders), the permeability – which reflects the microstructural characteristics – is significantly different. This result shows that the particle shape can be used as a design parameter in the event that the pressure drop is a limiting factor, a situation not at all uncommon in the industrial setting.

A comprehensive analysis of the effect of the microstructural properties of the two beds on the flow and transport shows that the dispersion is higher in the bed of spheres, and that the bed of cylinders, which has smaller pores in between the particles, exhibit larger variations in local concentration. These observations have implications for the formulation of reduced-order models, where local fluctuations are averaged out and need to be accounted for in some other fashion.

When a liquid phase is introduced into the beds, the microstructures are homogenized as the liquid tends to fill the smaller pores. This phenomenon leads to that the intermittent presence of a liquid reduces the differences between the two types of beds. It is also interesting to note that the shape and extent of the gas–liquid interface will be determined by the particle packing rather than by intrinsic particle

properties, pointing to that reduced-order evaporation models should reflect the microstructure of the relevant bed rather than be associated with the specific surface of the particles used. Finally, the effect of interstitial liquid on the streamwise velocity distributions in both beds is significant, indicating that reduced-order models should let the intermittent presence of liquid be reflected dynamically in the macroscopic description of the packed-bed adsorber.

Conflict of interest

None declared.

Declaration of Competing Interest

The authors report no declarations of interest.

Acknowledgements

This work has been financially supported by the Swedish Energy Agency (project number 41245-1) and the Swedish Centre for Biomass Gasification (SFC, project number P34721-3).

References

Allen, K.G., von Backström, T.W., Kröger, D.G., 2013. Packed bed pressure drop dependence on particle shape, size distribution, packing arrangement and roughness. Powder Technol. 246, 590–600.

Baranau, V., Tallarek, U., 2014. Random-close packing limits for monodisperse and polydisperse hard spheres. Soft Matter 10, 3826–3841.

Berryman, J.G., 1983. Random close packing of hard spheres and disks. Phys. Rev. A 27, 1053–1061.

2021. Blender. https://www.blender.org/.

Boccardo, G., Augier, F., Haroun, Y., Ferré, D., Marchisio, D., 2015. Validation of a novel open-source work-flow for the simulation of packed-bed reactors. Chem. Eng. J. 279, 809–820.

Brosillon, S., Manero, M.-H., Foussard, J.-N., 2001. Mass transfer in VOC adsorption on zeolite: experimental and theoretical breakthrough curves. Environ. Sci. Technol. 35 (17), 3571–3575.

De Anna, P., Dentz, M., Tartakovsky, A., Le, T., Borgne, 2014. The filamentary structure of mixing fronts and its control on reaction kinetics in porous media flows. Geophys. Res. Lett. 41 (13), 4586–4593.

De Maio, A., Palpacelli, S., Succi, S., 2011. A new boundary condition for three-dimensional lattice Boltzmann simulations of capillary filling in rough micro-channels. Commun. Comput. Phys. 9 (5), 1284–1292.

Deen, N.G., Peters, E.A.J.F., Padding, J.T., Kuipers, J.A.M., 2014. Review of direct numerical simulation of fluid-particle mass, momentum and heat transfer in dense gas-solid flows. Chem. Eng. Sci. 116, 710–724.

Dixon, A.G., 1988. Correlations for wall and particle shape effects on fixed bed bulk voidage. Can. J. Chem. Eng. 66, 705–708.

Dolamore, F., Dimartino, S., Fee, C.J., 2019. Numerical elucidation of flow and dispersion in ordered packed beds: nonspherical polygons and the effect of particle overlap on chromatographic performance. Anal. Chem. 91, 15009–15016.

Dorai, F., Teixeira, C.M., Rolland, M., Climent, E., Marcoux, M., Wachs, A., 2015. Fully resolved simulations of the flow through a packed bed of cylinders: effect of size distribution. Chem. Eng. Sci. 129, 180–192.

Gautier, R., Dbouk, T., Harion, J.-L., Hamon, L., Pré, P., 2018a. Pressure-swing-adsorption of gaseous mixture in isotropic porous medium: numerical sensitivity analysis in CFD. Chem. Eng. Res. Des. 129, 314–326.

Gautier, R., Dbouk, T., Campesi, M.A., Hamon, L., Harion, J.-L., Hamon, L., Pré, P., 2018b. Pressure-swing-adsorption of gaseous mixture in isotropic porous medium: transient 3D modeling and validation. Chem. Eng. J. 348, 1049–1062.

Gnielinski, V., 1978. Gleichungen zur berechnung des wärme-und stoffaustausches in durchströmten ruhenden kugelschuttungen bei mittleren und grossen pecletzahlen. Verfahrenstechnik 12 (6), 363–367.

Govender, N., Cleary, P.W., Kiani-Oshtorjani, M., Wilke, D.N., Wu, C.-Y., Kureck, H., 2020. The effect of particle shape on the packed bed effective thermal conductivity based on DEM with polyhedral particles on the GPU. Chem. Eng. Sci. 219, 115584.

Groen, D., Zasada, S.J., Coveney, P.V., 2014. Survey of multiscale and multiphysics applications and communities. Comput. Sci. Eng. 16, 34–43.

Guo, Z., Zheng, C., Shi, B., 2002. Discrete lattice effects on the forcing term in the lattice Boltzmann method. Phys. Rev. E 65 (4), 046308.

Habtu, N., Font, J., Fortuny, A., Bengoa, C., Fabregat, A., Haure, P., Ayude, A., Stüber, F., 2011. Heat transfer in trickle bed column with constant and modulated feed temperature: experiments and modeling. Chem. Eng. Sci. 66, 3358–3368.

Haddadi, B., Jordan, C., Norouzi, H.R., Harasek, M., 2016. Investigation of the pressure drop of random packed bed adsorbers. Chem. Eng. Trans. 52, 1–6.

Huang, J., Yong, W.-A., 2015. Boundary conditions of the lattice Boltzmann method for convection-diffusion equations. J. Comput. Phys. 300, 70–91.

Jareteg, A., Israelsson, M., Sasic, S., Thunman, H., Ström, H., 2017. Packed-bed reactor characterization of steam-regenerated solvent adsorbers for raw-gas cleaning. In: Proceedings of the 14th International Conference on Multiphase Flow in Industrial Plant, Desenzano del Garda, Italy, pp. 1–12.

Jareteg, A., Maggiolo, D., Larsson, A., Thunman, H., Sasic, S., Ström, H., 2020. Industrial-scale benzene adsorption: assessment of a baseline one-dimensional temperature swing model against online industrial data. Ind. Eng. Chem. Res. 59, 12239–12249.

Jareteg, A., 2021. Multi-Scale Analyses of Cycled Industrial-Scale Packed-Bed Adsorbers (Ph.D. thesis). Chalmers University of Technology.

Jin, Y., Makse, H.A., 2010. A first-order phase transition defines the random close packing of hard spheres. Physica A 389, 5362–5379.

Karthik, G.M., Buwa, V.V., 2016. Effect of particle shape on fluid flow and heat transfer for methane steam reforming reactions in a packed bed. AIChE J. 63, 366–377.

Khirevich, S., Daneyko, A., Höltzel, A., Seidel-Morgenstern, A., Tallarek, U., 2010. Statistical analysis of packed beds, the origin of short-range disorder, and its impact on eddy dispersion. J. Chromatogr. A 1217, 4713–4722.

Maggiolo, D., Seemann, M., Thunman, H., Santos, O., Larsson, A., Sasic, S., Ström, H., 2019. Self-cleaning surfaces for heat recovery during industrial hydrocarbon-rich gas cooling: an experimental and numerical study. AIChE J. 65 (1), 317–325.

Maggiolo, D., Picano, F., Zanini, F., Carmignato, S., Garnieri, M., Sasic, S., Ström, H., 2020. Solute transport and reaction in porous electrodes at high Schmidt numbers. J. Fluid Mech. 896 (A13), 1–28.

Mueller, G.E., 2005. Numerically packing spheres in cylinders. Powder Technol. 159, 105–110.

Nauman, E.B., Nigam, A., 2005. On axial diffusion in laminar-flow reactors. Ind. Eng. Chem. Res. 44 (14), 5031–5035.

Nawada, S., Dimartino, S., Fee, C., 2017. Dispersion behavior of 3D-printed columns with homogeneous microstructures comprising differing element shapes. Chem. Eng. Sci. 164, 90–98.

Nemec, D., Levec, J., 2005. Flow through packed bed reactors. 1. Single-phase flow. Chem. Eng. Sci. 60, 6947–6957.

Nouh, S.A., Lau, K.K., Shariff, A.M., 2010. Modeling and simulation of fixed bed adsorption column using integrated CFD approach. J. Appl. Sci. 10 (24), 3229–3235.

Onda, K., Takeuchi, H., Okumoto, Y., 1968. Mass transfer coefficients between gas and liquid phases in packed columns. J. Chem. Eng. Jpn. 1 (1), 56–62.
Peters, B., 2013. The extended discrete element method (XDEM) for multi-physics applications. Schol. J. Eng. Res.
Rabbani, A., Jamshidi, S., Salehi, S., 2014. An automated simple algorithm for realistic pore network extraction from micro-tomography images. J. Pet. Sci. Eng. 123, 164–171.
Rambabu, K., Muruganandam, L., Velu, S.C.F.D., 2014. CFD simulation for separation of carbon dioxide-methane mixture by pressure swing adsorption. Int. J. Chem. Eng. 2014, 402756.
Sbragaglia, M., Shan, X., 2011. Consistent pseudopotential interactions in lattice Boltzmann models. Phys. Rev. E. 84 (3), 036703.
Schulze, S., Nikrityuk, P., Compart, F., Richter, A., Meyer, B., 2017. Particle-resolved numerical study of char conversion processes in packed beds. Fuel 207, 655–662.
Schweiger, T.A.J., LeVan, M.D., 1993. Steam regeneration of solvent adsorbers. Ind. Eng. Chem. Res. 32 (10), 2418–2429.
Schweiger, T.A.J., 1996. A design method for adsorption bed capacity: steam-regenerated adsorbers. Ind. Eng. Chem. Res. 35 (6), 1929–1934.
Shan, X., Chen, H., 1993. Lattice Boltzmann model for simulating flows with multiple phases and components. Phys. Rev. E 47 (3), 1815.
Singhal, A., Cloete, S., Radl, S., Quinta-Ferreira, R., Amini, S., 2017. Heat transfer to a gas from densely packed beds of monodisperse spherical particles. Chem. Eng. J. 314, 27–37.
Succi, S., 2001. The Lattice Boltzmann Equation: For Fluid Dynamics and Beyond. Oxford University Press.
Tabib, M.V., Johansen, S.T., Amini, S., 2013. A 3D CFD-DEM methodology for simulating industrial scale packed bed chemical looping combustion reactors. Ind. Eng. Chem. Res. 52, 12041–12058.
Tavassoli, H., Peters, E.A.J.F., Kuipers, J.A.M., 2015. Direct numerical simulation of fluid-particle heat transfer in fixed random arrays of non-spherical particles. Chem. Eng. Sci. 129, 42–48.
Thaker, A.H., Karthik, G.M., Buwa, V.V., 2019. PIV measurements and CFD simulations of the particle-scale flow distribution in a packed bed. Chem. Eng. J. 374, 189–200.
Yang, C., Miao, G., Pi, Y., Xia, Q., Wu, J., Li, Z., Xiao, J., 2019. Abatement of various types of VOCs by adsorption/catalytic oxidation: a review. Chem. Eng. J. 370, 1128–1153.
Zare, M., Hashemabadi, S.H., 2020. Particle-fluid heat transfer close to the bed wall: CFD simulation and experimental study of particle shape influence on the formation of hot zones. Int. J. Therm. Sci. 150, 106223.
Zhang, J., Tian, F., 2008. A bottom-up approach to non-ideal fluids in the lattice Boltzmann method. Europhys. Lett. 81 (6), 66005.
Zhang, W., Thompson, K.E., Reed, A.H., Beenken, L., 2006. Relationship between packing structure and porosity in fixed beds of equilateral cylindrical particles. Chem. Eng. Sci. 61, 8060–8074.
Zou, R.P., Yu, A.B., 1995. The packing of spheres in a cylindrical container: the thickness effect. Chem. Eng. Sci. 50, 1504–1507.